

# Score-based diffusion models for accelerated MRI

Hyungjin Chung<sup>a</sup>, Jong Chul Ye<sup>a,\*</sup>

<sup>a</sup>Department of Bio and Brain Engineering, Korea Advanced Institute of Science and Technology (KAIST), Daejeon 34141, Republic of Korea

---

## ARTICLE INFO

---

2021 MSC: 92C55, 68U10, 34A55

Keywords:

Score-based models

Diffusion models

Inverse problems

MRI

---

## ABSTRACT

---

Score-based diffusion models provide a powerful way to model images using the gradient of the data distribution. Leveraging the learned score function as a prior, here we introduce a way to sample data from a conditional distribution given the measurements, such that the model can be readily used for solving inverse problems in imaging, especially for accelerated MRI. In short, we train a continuous time-dependent score function with denoising score matching. Then, at the inference stage, we iterate between numerical SDE solver and data consistency projection step to achieve reconstruction. Our model requires magnitude images only for training, and yet is able to reconstruct complex-valued data, and even extends to parallel imaging. The proposed method is agnostic to sub-sampling patterns, and can be used with any sampling schemes. Also, due to its generative nature, our approach can quantify uncertainty, which is not possible with standard regression settings. On top of all the advantages, our method also has very strong performance, even beating the models trained with full supervision. With extensive experiments, we verify the superiority of our method in terms of quality and practicality.

© 2021

---

## 1. Introduction

Reconstruction methods from sub-sampled measurements for magnetic resonance imaging (MRI) have been largely developed over the years. Iterative methods exploit sparsity of hand-crafted priors along with data consistency to arrive at a solution (Donoho, 2006), yet the construction of priors are often non-trivial, and *none* of them can properly model the actual complicated distribution of  $p(\mathbf{x})$ . Data-driven deep learning methods train the models either directly (Wang et al., 2016) or indirectly (Oh et al., 2020; Yaman et al., 2020), yet the methods rely heavily on supervision of well-curated large database of  $k$ -space data, which are hard to obtain.

Recently, score-based models (Hyvärinen and Dayan, 2005; Song and Ermon, 2019), and denoising diffusion probabilistic models (DDPMs) (Sohl-Dickstein et al., 2015; Ho et al., 2020) have gained wide interest as a new class of generative model which achieves surprisingly high sample quality without adversarial training (Song et al., 2021c; Nichol and Dhariwal, 2021; Dhariwal and Nichol, 2021). Among many works, (Song et al., 2021c) generalized discrete score-matching procedure with a continuous stochastic differential equation (SDE), which in fact also subsumes diffusion models into the same

framework. We refer to score-base SDEs as score-based diffusion models henceforth to emphasize that our proposed methodology can be flexibly used with any realizations from the two model classes.

Score-based diffusion models perturb the data distribution according to the forward SDE by injecting Gaussian noise, arriving at a tractable distribution (e.g. isotropic Gaussian distribution). In order to sample from data distribution, one can train a neural network to estimate the gradient of the log data distribution (i.e. score function,  $\nabla_{\mathbf{x}} \log p(\mathbf{x})$ ), and use it to solve the reverse SDE numerically. Unconditional generation of samples from  $p(\mathbf{x})$  using these score-based diffusion models have found their applications in image (Song et al., 2021c; Nichol and Dhariwal, 2021; Dhariwal and Nichol, 2021), audio (Kong et al., 2021), and even graph (Niu et al., 2020) synthesis. Conditional generation from  $p(\mathbf{x}|\mathbf{y})$  has also been studied in the context of widely known computer vision problems: in-painting (Song and Ermon, 2019; Song et al., 2021c), super-resolution (Choi et al., 2021; Saharia et al., 2021), and image editing (Meng et al., 2021).

In this work, we propose a framework generally applicable to solving inverse problems in imaging, and especially focus on the task of MRI reconstruction. The algorithm relies on projection onto convex sets (POCS), already extensively studied in the field of MRI reconstruction (Samsonov et al., 2004; Lustig and Pauly, 2010), and hence name our method score-

---

\*Corresponding author.

*e-mail:* jong.ye@kaist.ac.kr (Jong Chul Ye)

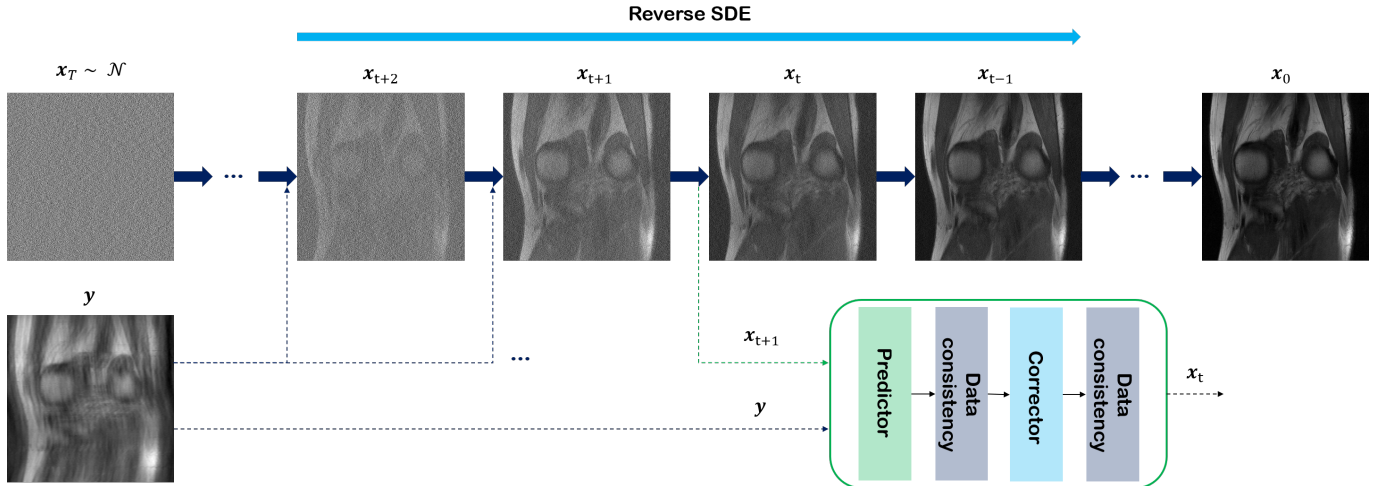


Fig. 1: Overview of the proposed method. Starting from  $x_T$ , sampled from the prior distribution,  $x_0$  is reached by solving the reverse SDE with Score-POCS sampling, alternating between the update step, and the data consistency step.

POCS. Notably, score-POCS requires training a *single* score function with *magnitude images only*, as in the earlier works targeting image generation. Despite the fact that the score function was not trained to solve the image reconstruction task, our method achieves state-of-the-art performance, even outperforming models that were trained in a supervised fashion specifically for image reconstruction task for complex images. Furthermore, our model is agnostic to the sub-sampling pattern used in the acceleration procedure, as opposed to supervised models which require re-training every time a new sampling scheme is designed. Finally, the proposed method can be extended to the reconstruction of complex-valued single-coil and multi-coil acquisition using a *single* network which has *never* seen complex-valued data before.

We train our network using the de-noising score matching loss for variance exploding (VE)-SDE (Song et al., 2021c). With the trained model at hand, we construct a solver for the reverse SDE, which enables us to sample from the distribution  $p(\mathbf{x}|\mathbf{y})$ , conditioned on the measurement  $\mathbf{y}$ . This is done by imposing projection-based data consistency step at every iteration, after the unconditional update step. Interestingly, we empirically found that by simply applying the score function to real and imaginary parts of the image separately, we are able to reconstruct complex-valued images. Even more, our method can be readily applied to practical multi-coil settings with the same score function using GRAPPA-type approach (Griswold et al., 2002), where the update via score function can be applied in parallel to each coil image. Overview of the proposed method is illustrated in Fig. 1, and we detail our proposed method in Section 3.

The proposed method is inherently stochastic, and for that we can sample multiple reconstruction results from the same measurement vector  $\mathbf{y}$ . This is especially useful since we are able to quantify uncertainty without any specific treatment (e.g. Monte Carlo dropout (Gal and Ghahramani, 2016), estimating variance directly (Kendall and Gal, 2017)) to the neural net. We observe that at low acceleration factors, posterior samples do not deviate much from each other, meaning high confidence

of the network. As acceleration factor is pushed to higher values, the variance gradually increases, which can potentially aid practitioners' decision making.

The manuscript is organized as follows: relevant background on score-based diffusion models is reviewed in Section 2; detailed procedure and algorithm of the proposed method, score-POCS, is presented in Section 3; specifications about the implementation and experiments are given in Section 4; experimental results are featured in Section 5; discussion about the concurrent works of conditional generation using diffusion models, limitations, and broader impacts of our work is presented in Section 6; we conclude our work in Section 7.

## 2. Background

### 2.1. Score-based SDE

One can construct a continuous diffusion process  $\{\mathbf{x}(t)\}_{t=0}^T$  with  $\mathbf{x}(t) \in \mathbb{R}^n$ , where  $t \in [0, T]$  is the time index of the progression and  $n$  denotes the image dimension. We choose  $\mathbf{x}(0) \sim p_{data}$  and  $\mathbf{x}(T) \sim p_T$ , where  $p_{data}, p_T$  refers to the data distribution of interest, and the prior distribution which are tractable to sample from (e.g. spherical Gaussian distribution), respectively. Then, the stochastic process can be constructed as the solution to the following SDE

$$d\mathbf{x} = \mathbf{f}(\mathbf{x}, t)dt + g(t)d\mathbf{w}, \quad (1)$$

where  $\mathbf{f} \in \mathbb{R}^n$  and  $g \in \mathbb{R}$  correspond to the drift coefficient, and the diffusion coefficient, respectively, and  $\mathbf{w} \in \mathbb{R}^n$  induces Brownian motion.

One can construct different SDEs by choosing different functions for  $\mathbf{f}$  and  $g$ . First, by choosing

$$\mathbf{f} = -\frac{1}{2}\beta(t)\mathbf{x}, \quad g = \sqrt{\beta(t)}, \quad (2)$$

where  $0 < \beta(t) < 1$  is a monotonically increasing function of noise scale, one achieves the variance preserving (VP)-SDE

(Ho et al., 2020). In this case, the magnitude of the signal decays to 0, and the variance is preserved to a fixed constant as  $t \rightarrow \infty$ . In fact, VP-SDE can be seen as the continuous version of DDPM (Song et al., 2021c; Kingma et al., 2021). Therefore, while DDPM was developed in a separate variational framework, it can also be seen as a realization of SDE.

On the other hand, variance exploding (VE) SDEs choose

$$\mathbf{f} = \mathbf{0}, \quad g = \sqrt{\frac{d[\sigma^2(t)]}{dt}} d\mathbf{w}, \quad (3)$$

where  $\sigma(t) > 0$  is again a monotonically increasing function, typically chosen to be a geometric series (Song and Ermon, 2019; Song et al., 2021c). Unlike VP-SDE, VE-SDE diffuses the signal with very large variance, which explodes as  $t \rightarrow \infty$ , hence its name. Empirically, we found that using VE-SDE typically leads to higher sample qualities, and hence focus on developing our method on top of VE-SDE hereafter. However, we note that the use of VP-SDE (including family of DDPMs developed under the variational framework) is also straightforward under our framework.

Interestingly, the reverse process of (1) can be constructed with another stochastic process (Song et al., 2021c):

$$\begin{aligned} d\mathbf{x} &= [\mathbf{f}(\mathbf{x}, t) - g(t)^2 \underbrace{\nabla_{\mathbf{x}} \log p_t(\mathbf{x})}_{\text{score function}}] dt + g(t) d\bar{\mathbf{w}} \quad (4) \\ &= \frac{d[\sigma^2(t)]}{dt} \underbrace{\nabla_{\mathbf{x}} \log p_t(\mathbf{x})}_{\text{score function}} + \sqrt{\frac{d[\sigma^2(t)]}{dt}} d\bar{\mathbf{w}}, \end{aligned}$$

where  $dt$  is the infinitesimal *negative* time step, and  $\bar{\mathbf{w}}$  is the Brownian motion running backwards. The last equality follows by plugging in Eq. (3) to Eq. (4).

In order to solve (4), one has to know the score function for all  $t$ . One can estimate this score function with a time-conditional neural network  $s_\theta(\mathbf{x}, t) \simeq \nabla_{\mathbf{x}} \log p_t(\mathbf{x}(t))$ , and replace the term in (4). Since we do not know the *true* score, we can instead use denoising score matching (Vincent, 2011), where we replace the unknown  $\nabla_{\mathbf{x}} \log p_t(\mathbf{x})$  with  $\nabla_{\mathbf{x}} \log p_{0t}(\mathbf{x}(t)|\mathbf{x}(0))$ , where  $p_{0t}(\mathbf{x}(t)|\mathbf{x}(0))$  is the Gaussian perturbation kernel centered at  $\mathbf{x}(0)$ . Under some regularity conditions,  $s_\theta$  trained with denoising score matching will satisfy  $s_{\theta^*}(\mathbf{x}, t) = \log p_t(\mathbf{x}(t))$  almost surely (Song et al., 2020). Formally, we optimize the parameters  $\theta$  of the score network with the following cost:

$$\begin{aligned} \min_{\theta} \mathbb{E}_{t \sim U(0,1)} \left[ \lambda(t) \mathbb{E}_{\mathbf{x}(0)} \mathbb{E}_{\mathbf{x}(t)|\mathbf{x}(0)} \left[ \right. \right. \\ \left. \left. \left\| s_\theta(\mathbf{x}(t), t) - \nabla_{\mathbf{x}} \log p_{0t}(\mathbf{x}(t)|\mathbf{x}(0)) \right\|_2^2 \right] \right]. \quad (5) \end{aligned}$$

In the case of Gaussian perturbation kernels, the gradient of the perturbation kernel can be formulated explicitly:  $\nabla_{\mathbf{x}} \log p_{0t}(\mathbf{x}(t)|\mathbf{x}(0)) = (\mathbf{x}(t) - \mathbf{x}(0))/\sigma(t)^2$ . Intuitively, one can also understand (5) as training the neural network to de-noise  $\mathbf{x}(t)$ , which was constructed by adding noise to  $\mathbf{x}(0)$ .

Once the network is trained with (5), we can plug the approximation  $s_\theta(\mathbf{x}, t) \simeq \nabla_{\mathbf{x}} \log p_t(\mathbf{x}(t))$  to solve the reverse SDE in Eq. (4):

$$d\mathbf{x} = \frac{d[\sigma^2(t)]}{dt} s_\theta(\mathbf{x}, t) + \sqrt{\frac{d[\sigma^2(t)]}{dt}} d\bar{\mathbf{w}}. \quad (6)$$

Then, we can solve the SDE numerically, for example, with Euler discretization (Song et al., 2021c). This involves discretizing  $t$  in range  $[0, 1]$  uniformly into  $N$  intervals such that  $0 = t_0 < t_1 < \dots < t_N = 1$ , with  $\Delta t = 1/N$ . Additionally, we can correct the direction of gradient ascent with *corrector* algorithms such as Langevin MC (Parisi, 1981). Iteratively applying predictor and corrector steps yield the predictor-corrector (PC) sampling algorithm (Song et al., 2021c), as presented in Algorithm 1. With the algorithm presented in Algorithm 1, we can sample from the distribution  $p(\mathbf{x})$ . In Section 3, we extend this sampling scheme to a conditional sampling algorithm, which enables us to sample from  $p(\mathbf{x}|\mathbf{y})$ .

---

#### Algorithm 1 Predictor-Corrector (PC) sampling

---

**Require:**  $s_\theta, N, M, \{\epsilon_i\}$      $\triangleright$  step size,  $\{\sigma_i\}$      $\triangleright$  noise schedule

- 1:  $\mathbf{x}_N \sim \mathcal{N}(\mathbf{0}, \sigma_T^2 \mathbf{I})$
- 2: **for**  $i = N - 1 : 0$  **do**
- 3:     $\mathbf{x}'_i \leftarrow \mathbf{x}_{i+1} + (\sigma_{i+1}^2 - \sigma_i^2) s_\theta(\mathbf{x}_{i+1}, \sigma_{i+1})$
- 4:     $\mathbf{z} \sim \mathcal{N}(\mathbf{0}, \mathbf{I})$
- 5:     $\mathbf{x}_i \leftarrow \mathbf{x}'_i + \sqrt{\sigma_{i+1}^2 - \sigma_i^2} \mathbf{z}$      $\left. \vphantom{\mathbf{x}_i} \right\}$  Predictor
- 6:    **for**  $j = 1 : M$  **do**
- 7:      $\mathbf{z} \sim \mathcal{N}(\mathbf{0}, \mathbf{I})$
- 8:      $\mathbf{x}'_i \leftarrow \mathbf{x}_i + \epsilon_j s_\theta(\mathbf{x}_i, \sigma_i)$
- 9:      $\mathbf{x}_i \leftarrow \mathbf{x}'_i + \sqrt{2\epsilon_j} \mathbf{z}$      $\left. \vphantom{\mathbf{x}_i} \right\}$  Corrector
- 10:    **end for**
- 11: **end for**
- 12: **return**  $\mathbf{x}_0$

---

### 3. Main Contributions

#### 3.1. Forward Measurement Model

In accelerated MRI, we consider the following measurement model

$$\mathbf{y} = A\mathbf{x} \quad (7)$$

where  $\mathbf{y} \in \mathbb{R}^m$  is the measurement,  $\mathbf{x} \in \mathbb{R}^n$  is the latent image, and a parameterized forward measurement matrix  $A \in \mathbb{R}^{m \times n}$  is defined as

$$A_\Omega := \mathcal{P}_\Omega \mathcal{F} \mathcal{S}, \quad (8)$$

where  $\mathcal{S} := [\mathcal{S}^{(1)}; \dots; \mathcal{S}^{(c)}]$  is the sensitivity map for  $c$  different coils,  $\mathcal{F}$  denotes Fourier transform, and  $\mathcal{P}_\Omega$  is the sub-sampling operator with the given sampling pattern  $\Omega$ . In the case of single-coil acquisition,  $\mathcal{S}$  reduces to identity matrix such that  $A_\Omega = \mathcal{P}_\Omega \mathcal{F}$ .

#### 3.2. Reverse SDE for Accelerated MR Reconstruction

A classic approach to find the solution of Eq. (7) is to solve the following constrained optimization problem:

$$\begin{aligned} \min_{\mathbf{x}} \quad & \Psi(\mathbf{x}) \quad (9) \\ \text{subject to} \quad & \mathbf{y} = A_\Omega \mathbf{x}, \end{aligned}$$

where  $\Psi(\cdot)$  is, for example, a sparsity promoting regularizer derived from compressed sensing (CS) theory (Donoho, 2006),

**Algorithm 2** Score-POCS sampling (Real)

---

**Require:**  $s_\theta, N, M, \{\epsilon_i\}$   $\triangleright$  step size,  $\{\sigma_i\}$   $\triangleright$  noise schedule  
**Define**  $A_\Omega := \mathcal{P}_\Omega \mathcal{F}$   
1:  $\mathbf{x}_N \sim \mathcal{N}(\mathbf{0}, \sigma_N^2 \mathbf{I})$   
2: **for**  $i = N - 1 : 0$  **do**  
3:    $\mathbf{x}_i \leftarrow \text{Predictor}(\mathbf{x}_{i+1}, \sigma_i, \sigma_{i+1})$   
4:    $\mathbf{x}_i \leftarrow \text{Re}(A_{\Omega^c}^* A_{\Omega^c} \mathbf{x}_i + A_{\Omega^c}^* \mathbf{y})$   
5:   **for**  $j = 1 : M$  **do**  
6:      $\mathbf{x}_i \leftarrow \text{Corrector}(\mathbf{x}_i, \sigma_i, \epsilon_i)$   
7:      $\mathbf{x}_i \leftarrow \text{Re}(A_{\Omega^c}^* A_{\Omega^c} \mathbf{x}_i + A_{\Omega^c}^* \mathbf{y})$   
8:   **end for**  
9: **end for**  
10: **return**  $\mathbf{x}_0$

---

such as  $\ell_1$  wavelet (Lustig et al., 2007) and total variation (TV) (Block et al., 2007). Solving Eq. (9) typically involves proximal algorithms such as variable splitting (Boyd et al., 2011) or projection onto the convex sets (POCS) (Samsonov et al., 2004), which decouples the optimization of the prior term, and the forward consistency term. Then, one can alternate between solving the two sub-problems to arrive at the optimum.

In Bayesian perspective, we immediately see that  $\Psi(\mathbf{x})$  in Eq. (9) is the prior model of the data, i.e.  $p(\mathbf{x})$ . Hence, we can imagine that by more accurately estimating the complex prior data distribution, one would be able to achieve higher quality samples.

That being said, one of the important differences of the proposed method compared to the classical approaches is that rather than modeling the prior distribution  $p(\mathbf{x})$ , we exploit its stochastic samples. Specifically, the samples from the prior distribution can be obtained from the reverse SDE in Eq. (4), which can be discretized as illustrated in Algorithm 1 with

$$\mathbf{x}_i = (\sigma_{i+1}^2 - \sigma_i^2) s_\theta(\mathbf{x}_{i+1}, \sigma_{i+1}) + \sqrt{\sigma_{i+1}^2 - \sigma_i^2} \mathbf{z}, \quad (10)$$

Then, the projection on the constraint in (9) can be implemented by

$$\mathbf{x}_i = A_{\Omega^c}^* A_{\Omega^c} \mathbf{x}_i + A_{\Omega^c}^* \mathbf{y}, \quad (11)$$

which effectively imposes data consistency by replacing the current estimate within  $\Omega$  with the known values of  $\mathbf{y}$ . This is also referred to as data consistency projection step. Application of Eqs. (10) and (11) correspond to the predictor step.

When using the additional corrector steps as in Algorithm 1, one can also apply the same treatment to the discrete corrector step

$$\begin{aligned} \mathbf{x}_i &= \mathbf{x}_{i+1} + \epsilon_i s_\theta(\mathbf{x}_{i+1}, \sigma_{i+1}) + \sqrt{2\epsilon_i} \mathbf{z} \\ \mathbf{x}_i &= A_{\Omega^c}^* A_{\Omega^c} \mathbf{x}_i + A_{\Omega^c}^* \mathbf{y}, \end{aligned} \quad (12)$$

where  $\epsilon_i$  is the step size at the  $i^{\text{th}}$  iteration. Iteratively applying predictor and corrector steps as in PC algorithm gives rise to the inference algorithm for our score-POCS, which is described formally in Algorithm 2.

Unfortunately, this algorithm can be used when we know a priori that the signal only contains real values, and care must

**Algorithm 3** Score-POCS sampling (SENSE-type)

---

**Require:**  $s_\theta, N, M, \{\epsilon_i\}$   $\triangleright$  step size,  $\{\sigma_i\}$   $\triangleright$  noise schedule  
1: **if** parallel imaging (PI) **then**  
2:    $A_\Omega := \mathcal{P}_\Omega \mathcal{F} \mathcal{S}$   
3: **else**  
4:    $A_\Omega := \mathcal{P}_\Omega \mathcal{F}$   
5: **end if**  
6:  $\mathbf{x}_N \sim \mathcal{N}(\mathbf{0}, \sigma_N^2 \mathbf{I})$   
7: **for**  $i = N - 1 : 0$  **do**  
8:    $\text{Re}(\mathbf{x}_i) \leftarrow \text{Predictor}(\text{Re}(\mathbf{x}_{i+1}), \sigma_i, \sigma_{i+1})$   
9:    $\text{Im}(\mathbf{x}_i) \leftarrow \text{Predictor}(\text{Im}(\mathbf{x}_{i+1}), \sigma_i, \sigma_{i+1})$   
10:    $\mathbf{x}_i = \text{Re}(\mathbf{x}_i) + \iota \text{Im}(\mathbf{x}_i)$   
11:    $\mathbf{x}_i \leftarrow A_{\Omega^c}^* A_{\Omega^c} \mathbf{x}_i + A_{\Omega^c}^* \mathbf{y}$   
12:   **for**  $j = 1 : M$  **do**  
13:      $\text{Re}(\mathbf{x}_i) \leftarrow \text{Corrector}(\text{Re}(\mathbf{x}_i), \sigma_i, \epsilon_i)$   
14:      $\text{Im}(\mathbf{x}_i) \leftarrow \text{Corrector}(\text{Im}(\mathbf{x}_i), \sigma_i, \epsilon_i)$   
15:      $\mathbf{x}_i = \text{Re}(\mathbf{x}_i) + \iota \text{Im}(\mathbf{x}_i)$   
16:      $\mathbf{x}_i \leftarrow A_{\Omega^c}^* A_{\Omega^c} \mathbf{x}_i + A_{\Omega^c}^* \mathbf{y}$   
17:   **end for**  
18: **end for**  
19: **return**  $\mathbf{x}_0$

---

be taken since in most practical situations of MRI reconstruction, the signal that we would like to reconstruct is complex. This introduces a caveat when reconstructing the data with the score function, because the original theory of score-based SDEs (Song et al., 2021c) were not developed to handle complex signals.

One approach that is feasible is to train a score function so that it handles complex signal, was proposed in (Ramzi et al., 2020). Implementation-wise, this corresponds to considering real and imaginary parts of the signal as separate channels, and applying the de-noising score matching objective to handle  $2 \times H \times W$  sized image, where  $H$  and  $W$  are the height, and the width of the image, respectively. However, we empirically found that this treatment reduces the stability of network training, and also hurts performance of the reconstruction using Algorithm 2. We further note that this treatment limits the practicality, since the model now requires raw  $k$ -space data for training.

To overcome these limitations, we propose a simple fix to Algorithm 2, which provides a way to use the score function  $s_\theta$  trained with magnitude images *only*, and use it to reconstruct complex images. The method is presented in Algorithm 3, where we split the image into real and imaginary parts, and apply the predictor-corrector step separately to each part. Accordingly, we can use the same score function that was trained with magnitude images to deal with complex image data in a seamless way. This simple fix works surprisingly well, and we show in Section 5.2 that reconstruction of complex-valued coil data with Algorithm 3 even outperforms the standard feed-forward neural network trained with explicit supervision. Being able to utilize score function trained with magnitude-only data to reconstruct complex-valued data is a great advantage, since we can use only the DICOM data to train the neural network. This is advantageous because plethora of MR scans exist in the form of DICOM (Zbontar et al., 2018), while the raw  $k$ -space data

**Algorithm 4** Score-POCS sampling (GRAPPA-type)

---

**Require:**  $s_\theta, N, M, \{\epsilon_i\}$   $\triangleright$  step size,  $\{\sigma_i\}$   $\triangleright$  noise schedule  
**Define**  $A_\Omega := \mathcal{P}_\Omega \mathcal{F}$

- 1: **for**  $c = 1 : N$  **do** (parallelizable)
- 2:    $\mathbf{x}_N^{(c)} \sim \mathcal{N}(\mathbf{0}, \sigma_T^2 \mathbf{I})$
- 3:   **for**  $i = N - 1 : 0$  **do**
- 4:      $\text{Re}(\mathbf{x}_i^{(c)}) \leftarrow \text{Predictor}(\text{Re}(\mathbf{x}_{i+1}^{(c)}), \sigma_i, \sigma_{i+1})$
- 5:      $\text{Im}(\mathbf{x}_i^{(c)}) \leftarrow \text{Predictor}(\text{Im}(\mathbf{x}_{i+1}^{(c)}), \sigma_i, \sigma_{i+1})$
- 6:      $\mathbf{x}_i = \text{Re}(\mathbf{x}_i) + \iota \text{Im}(\mathbf{x}_i)$
- 7:      $\mathbf{x}_i \leftarrow A_{\Omega^c}^* A_{\Omega^c} \mathbf{x}_i + A_{\Omega^c}^* \mathbf{y}$
- 8:     **for**  $j = 1 : M$  **do**
- 9:       $\text{Re}(\mathbf{x}_i^{(c)}) \leftarrow \text{Corrector}(\text{Re}(\mathbf{x}_i^{(c)}), \sigma_i, \epsilon_i)$
- 10:       $\text{Im}(\mathbf{x}_i^{(c)}) \leftarrow \text{Corrector}(\text{Im}(\mathbf{x}_i^{(c)}), \sigma_i, \epsilon_i)$
- 11:       $\mathbf{x}_i = \text{Re}(\mathbf{x}_i) + \iota \text{Im}(\mathbf{x}_i)$
- 12:       $\mathbf{x}_i \leftarrow A_{\Omega^c}^* A_{\Omega^c} \mathbf{x}_i + A_{\Omega^c}^* \mathbf{y}$
- 13:     **end for**
- 14:   **end for**
- 15: **end for**
- 16:  $\mathbf{x}_0 = \sqrt{\sum_{k=1}^c |\mathbf{x}_0^{(k)}|^2}$   $\triangleright$  SSOS
- 17: **return**  $\mathbf{x}_0$

---

are usually discarded due to memory issues.

### 3.3. Diffusion model meets Parallel Imaging (PI)

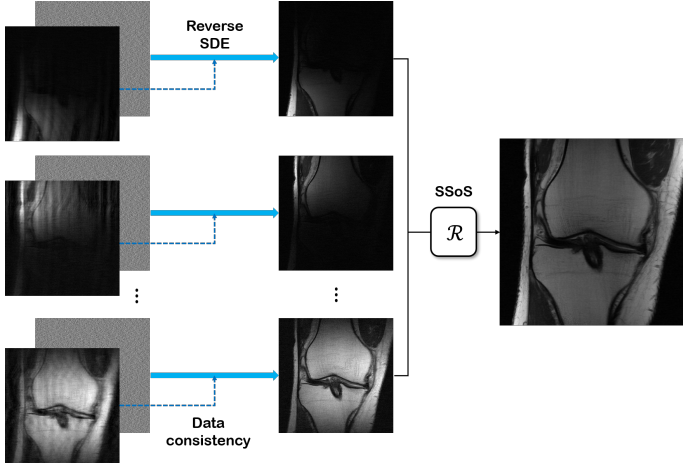


Fig. 2: Illustration of score-POCS applied to parallel imaging. Coil images are reconstructed separately, then merged with the SSOS operation.

While the proposed score-POCS framework for the reconstruction of complex-valued data is extremely useful, most modern MRI scanners (Zbontar et al., 2018) have *multiple* receiver coils, which capture signal with different sensitivities. Since the birth of PI (Deshmane et al., 2012), myriad of techniques to reconstruct the true latent signal have been proposed in literature, two of the most prominent being SENSE (Pruessmann et al., 1999), and GRAPPA (Griswold et al., 2002). Here, we show that score-POCS can be integrated seamlessly into GRAPPA.

Specifically, as introduced in Algorithm 4, our objective is to reconstruct the data coil-by-coil. However, unlike GRAPPA,

we need not estimate the GRAPPA kernels, but simply apply Algorithm 3 separately to each coil image, as illustrated in Fig. 2. Notably, although our score function estimator  $s_\theta(\mathbf{x}, t) \simeq \nabla_{\mathbf{x}} \log p(\mathbf{x})$  were not trained with separate coil images, since the distribution of independent coil images does not deviate much from  $p(\mathbf{x})$ , simply applying Algorithm 3 to each coil image induces very accurate reconstruction. Once this is done, we arrive at the final result with SSOS operation.

One caveat for the GRAPPA-type approach is the slow inference speed. Naively implementing GRAPPA-type score-POCS will induce  $c$  times longer computation time compared to the single-coil reconstruction. However, this can be much relieved by performing parallel computation with each coil data, since no computation needs to be shared across the threads. Given sufficient GPU resources, we expect that the computation time needed for reconstruction using this GRAPPA-type approach will be reduced down to the time needed for single-coil reconstruction.

## 4. Methods

### 4.1. Experimental data

All experiments were performed with fastMRI knee dataset (Zbontar et al., 2018), which is publicly available<sup>1</sup>. We trained the network with  $320 \times 320$  size target image magnitude, given as the key `reconstruction_esc`. We note that it is possible to train the score function with the same target from `reconstruction_rss` of the multi-coil dataset, but we found no significant difference in the performance.

Among 973 volumes of training data, we dropped the first and last five slices from each volume, to avoid training the model with noise-only data. This results in approximately 25k slices of training data. For testing, we randomly sampled 12 volumes from the validation set, and dropped the first and last 5 slices from each volume.

### 4.2. Implementation details

We follow similar procedures to train VE-SDE as advised in (Song et al., 2021c). Specifically, we train the network with the objective given in Eq. (5), with setting  $\lambda(t) = \sigma^2(t)$ . Note that this specific choice of  $\lambda(t)$  stabilizes the noise scale across  $t$ , and theoretically corresponds to likelihood weighting, as proven in (Song et al., 2021b). Plugging in the weighting function, we can train the model with the following cost:

$$\min_{\theta} \mathbb{E}_{t \sim U(\epsilon, 1)} \mathbb{E}_{\mathbf{x}(0) \sim p_0} \mathbb{E}_{\mathbf{x}(t) \sim \mathcal{N}(\mathbf{x}(0), \sigma^2(t) \mathbf{I})} \left[ \left\| \sigma(t) s_\theta(\mathbf{x}(t), t) - \frac{\mathbf{x}(t) - \mathbf{x}(0)}{\sigma(t)} \right\|_2^2 \right], \quad (13)$$

with setting  $\epsilon = 10^{-5}$  to circumvent numerical issues.

For the step size  $\epsilon_i$  used in the Langevin MC corrector step, we follow what is advised in (Song et al., 2021c), and set

$$\epsilon_i = 2r \frac{\|\mathbf{z}\|_2}{\|s_\theta(\mathbf{x}_i, \sigma_i)\|_2}, \quad (14)$$

<sup>1</sup><https://fastmri.org/>

where  $r = 0.16$  is set to a constant value. For noise variance schedule, we fix  $\sigma_{min} = 0.01, \sigma_{max} = 378$ , which is similar to what is advised in the technique of (Song and Ermon, 2020), then take the geometric series with the following form:

$$\sigma(t) = \sigma_{min} \left( \frac{\sigma_{max}}{\sigma_{min}} \right)^t. \quad (15)$$

We take the batch size of 1, and optimize the network using Adam optimizer ( $\beta_1 = 0.9, \beta_2 = 0.999$ ). We use linear warm-up schedule for the parameters for the first 5000 steps of optimization, reaching  $2e-4$  at the 5000<sup>th</sup> step. We apply gradient clipping with the maximum value of 1.0 (Arjovsky et al., 2017). Exponential moving average with rate 0.999 is applied to the parameters. Optimization was performed for 100 epochs, and it took about 3 weeks of training the score function with a single RTX 3090 GPU. All code was implemented in PyTorch (Paszke et al., 2019).

For all algorithms, we use  $N = 2000, M = 1$  iterations for inference as default, unless specified otherwise. Single forward-pass through  $s_\theta$  is required for both predictor and corrector steps, which takes about 150 ms with a commodity GPU. Summing up, this results in about 10 minutes of reconstruction time for real-valued images, and 20 minutes of reconstruction time for complex-valued images. We discuss ways for speeding up inference, and some potential directions of future studies in Section 6.3.

### 4.3. Model Architecture

We base the implementation of the time-dependent score function model `ncsnpp`<sup>2</sup> as suggested in (Song et al., 2021c). The model architecture stems from U-Net (Ronneberger et al., 2015), and the sub-block which consist U-Net are adopted from residual blocks of BigGAN (Brock et al., 2019). The skip connections in the residual blocks are scaled by  $1/\sqrt{2}$  as in (Karras et al., 2017, 2019, 2020). For pooling and unpooling, we adopt anti-aliasing pooling of (Zhang, 2019). The resulting U-Net has 4 different levels of scale, with 4 residual networks at each level. Conditioning of network with the time index  $t$  is performed with Fourier features (Tancik et al., 2020), where the conditional features are added to the encoder features.

### 4.4. Baseline Comparisons

To verify superiority over the current standards, we perform comparison studies with baseline methods used in (Zbontar et al., 2018). We choose total variation (TV) reconstruction (Block et al., 2007) as the representative CS reconstruction method, where we use the implementation in `sigpy.mri.app.TotalVariationRecon`<sup>3</sup>. We perform grid search on the hyper-parameter `lambda`, and report only the best results among them.

For representative deep learning approach, we use supervised learning-based reconstruction using U-Net (Zbontar et al.,

2018). While we could use the open-sourced<sup>4</sup> pre-trained model, we re-implemented the model to achieve better performance.

### 4.5. Measurement of Reconstruction Quality

To quantify the proximity of the reconstructions to the target, we use the standard 2 metrics - peak signal-to-noise ratio (PSNR), and structural similarity index (SSIM). While these are the two most widely used metrics in the community, it is also well known that these metrics hardly line up with the radiologists' scoring on the image quality (Mason et al., 2019).

To fully capture the superiority of the proposed method, we focus on the fact that *good* reconstructions are the ones that can be used for *accurate diagnosis*. If the reconstruction quality closely matches the ground truth, there should be no degeneration in the performance of the downstream tasks - in our case diagnosis. In order to compare against ground truth, the diagnostic ability of each reconstruction, we leverage the recent fastMRI+ (Zhao et al., 2021) dataset. For fastMRI knee data, fastMRI+ annotations provide bounding boxes around the pathologic region. We train a standard object detection model using the ground truth (fully sampled) images, and use this network to compare how well the model performs on pathology detection with reconstructions using different methods. For detailed experimental procedures, see the following section, i.e. Section 4.6. From the experiments, we quantify three standard metrics from the object detection literature - mean average precision (mAP), precision, and recall.

### 4.6. Pathology Detection

For the object detection model, we use the state-of-the-art YOLO v5<sup>5</sup>. We use the default configuration of `YOLOv5m`, which is a medium-sized model, often suggested as the baseline model when you do not have sufficient amount of data. When trying to fit larger versions of the model, namely `YOLOv5l`, `YOLOv5x`, etc, we found that overfitting occurs and the performance drops by a small margin.

For training data of the YOLOv5 model, we use all the training data with annotations in fastMRI+, which consists of 8053 images in total. We do not include any images without annotations in the training set. For testing, we select 4 random cases out of the validation set, which consists of 45 images in total.

Model weights were fine-tuned from the open-source pre-trained model, and were trained for 300 epochs using the batch size of 16. Training took about a day on 2×2080Ti GPU.

## 5. Results

### 5.1. Real-valued Simulation study

First, we show the results of the simulation study using respectively under-sampled fastMRI real-valued data of size 320×320 in Fig. 3. In the first row, we see reconstructions from 2D ×8 Gaussian random sampling, which is the sub-sampling

<sup>2</sup>[https://github.com/yang-song/score\\_sde\\_pytorch](https://github.com/yang-song/score_sde_pytorch)

<sup>3</sup><https://github.com/mikgroup/sigpy>

<sup>4</sup><https://github.com/facebookresearch/fastMRI>

<sup>5</sup><https://github.com/ultralytics/yolov5>

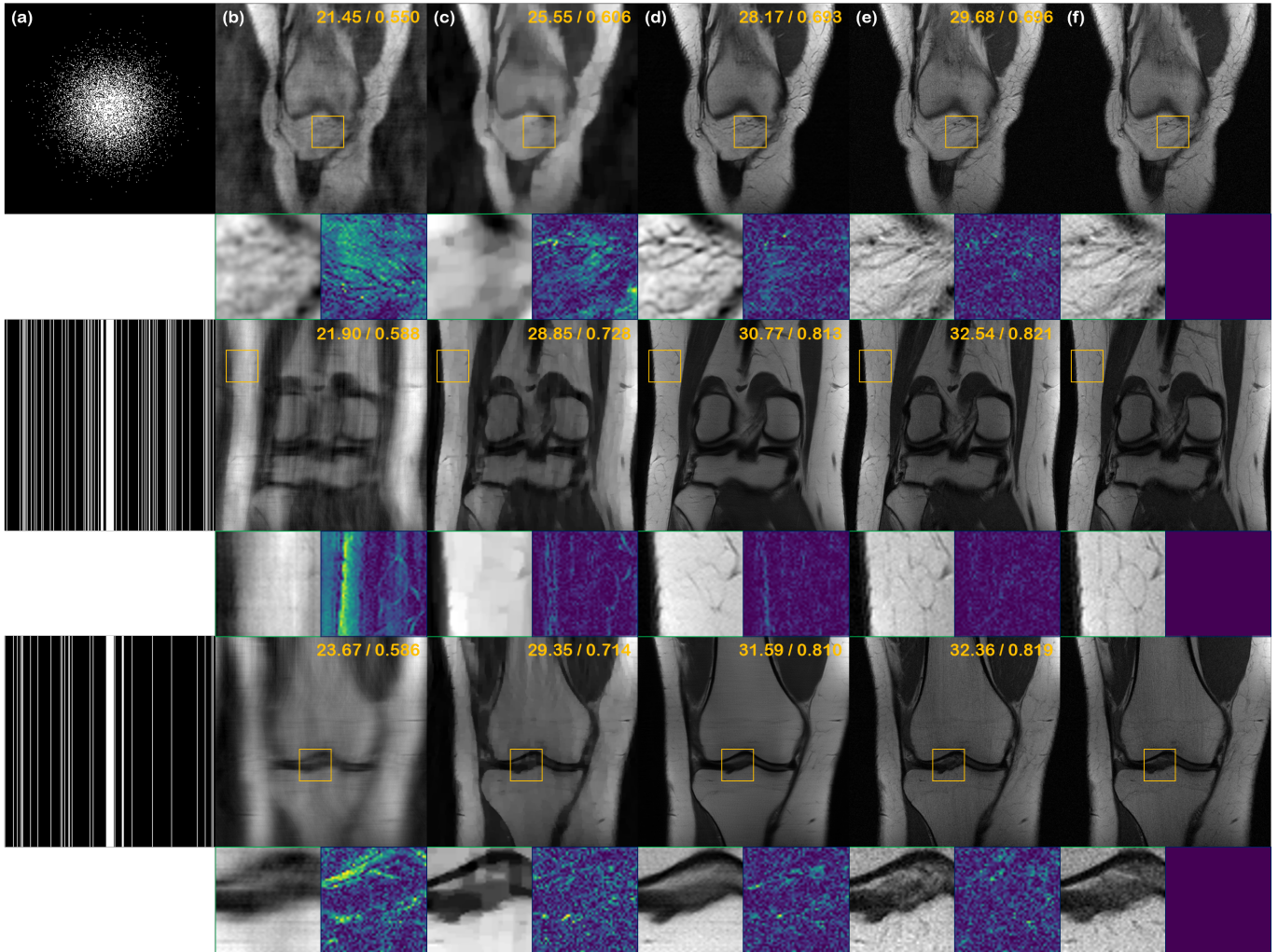


Fig. 3: Reconstructions of the real-valued simulation study. (a) Sub-sampling mask used to generate under-sampled image, (b) zero-filled reconstruction, (c) TV, (d) supervised learning (U-Net), (e) proposed method, and (f) ground truth. 1<sup>st</sup> row: 2D  $\times$ 8 Gaussian random sampling, 2<sup>nd</sup> row: 1D  $\times$ 4 uniform random sampling, 3<sup>rd</sup> row: 1D  $\times$ 8 uniform random sampling. Green box: Zoom in version of the indicated yellow box, Blue box: Difference magnitude of the inset (In Viridis colormap). Yellow numbers in the upper right corner indicate PSNR [db], and SSIM, respectively.

pattern which induces the least aliasing artifact. Here, we see that the proposed performs nearly perfect reconstruction, where we see virtually no structural difference even in the zoomed-in image. Reconstruction through total variation (TV) induces cartoon-like artifacts, and cannot remove the overall foggy artifacts across the whole image. Supervised method via U-Net produces satisfactory results, but of lower resolution compared to the ground truth.

On the second row, we compare the reconstructions from acceleration using  $\times$ 4 uniform random sampling with 4% of the phase encoding lines kept as the autocalibrating signal (ACS) region, producing moderate aliasing artifact. Even at this level, score-POCS is able to provide accurate reconstruction, capturing most of the high frequency details of the ground truth. In this acceleration factor, TV is not able to completely remove the aliasing artifacts. The averaging effect of supervised reconstruction now becomes more clear, often omitting the important details of the scan.

The last row shows the most aggressive acceleration factor -  $\times$ 8 uniform random sampling (4% ACS region), at which

we see that the image is severely degraded with artifacts. TV only partially removes the artifacts, while introducing quite an amount of cartoon-like artifacts. Supervised DL method smooths away a lot of details, producing unrealistic texture. Surprisingly, even at this level of acceleration factor, our method reconstructs fairly accurate reconstruction, matching most of the details from the ground truth.

We provide thorough comparison of quantitative metrics on the test set in Table 1. On all the different sampling patterns, score-POCS significantly outperform the comparison methods. For fair comparison, supervised U-Net models were trained for all the different sampling patterns - uniform 1D, Gaussian 1D, and Gaussian 2D. When we tried running a single model on different type of sampling pattern, U-Net model performed much worse. Contrarily, we use a single model for the proposed method.

It is worth mentioning the overall difference between the reconstructions through supervised U-Net, and the proposed method. We observe that the reconstructions using supervised U-Net becomes blurrier as we push the acceleration factor to

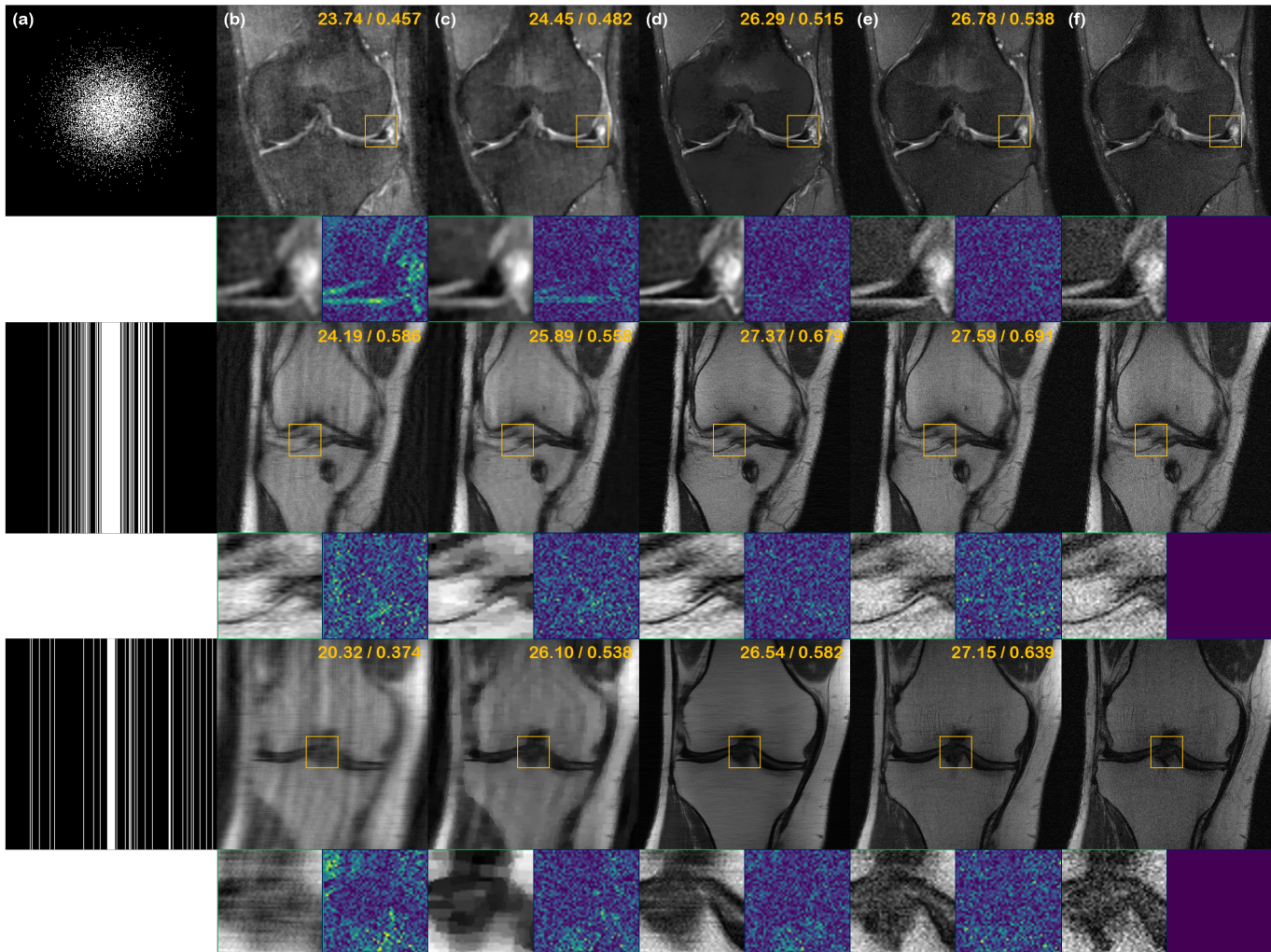


Fig. 4: Single-coil reconstruction results. (a) Sub-sampling mask used to generate under-sampled image, (b) zero-filled reconstruction, (c) TV, (d) supervised learning (U-Net), (e) proposed method, and (f) ground truth. 1<sup>st</sup> row: 2D  $\times$ 8 Gaussian random sampling, 2<sup>nd</sup> row: 1D  $\times$ 4 Gaussian random sampling, 3<sup>rd</sup> row: 1D  $\times$ 8 uniform random sampling. Green box: Zoom in version of the indicated yellow box, Blue box: Difference magnitude of the inset (In *Viridis* colormap). Yellow numbers in the upper right corner indicate PSNR [db], and SSIM, respectively.

higher values. This is a widely known effect for models that are trained with supervision using L1 loss, L2 loss, etc (Ledig et al., 2017); Typically, this behavior stems from the models collapsing to a single mode of the distribution, whereas the actual distribution is highly multi-modal. On the contrary, score-POCS does not show such effect, visiting the modes of high probability at each sample. For that matter, our method is able to 1) reconstruct high-frequency details even at high acceleration factors, and 2) quantify uncertainty, as we discuss in depth in Section 5.5

### 5.2. Complex-valued Single-coil Reconstruction

In Fig. 4, we illustrate the reconstruction results of the proposed method using Algorithm 3, along with the baseline comparisons. In the first row, we have  $\times$ 8 2D Gaussian random sampling acceleration. The proposed method performs nearly perfect reconstruction, without inducing any additional blurriness from the reconstruction process. TV, and supervised U-Net falls largely behind the proposed method both in terms of perceptual quality and the quantitative metrics.

In the second row, we have  $\times$ 4 1D Gaussian random sampling (8% ACS region) acceleration. Again, the proposed method reconstructs the aliased image with high accuracy, and has higher quality than the comparison methods.

The third row shows  $\times$ 8 1D uniform random sampling (4% ACS region). The proposed method is still able to reconstruct the aliased image with virtually no degradation in the high-frequency details. On the other hand, supervised U-Net reconstruction produces horizontal strip artifacts, hampering the visual quality. TV hardly produces satisfactory result. Quantitative metrics in Table 1 also confirm the superiority.

As mentioned earlier, all the results depicted in Fig. 4 were generated using the single score function, trained with DICOM images only. This means that the model has never seen complex-valued data before, and yet the quality of reconstruction is surprisingly high. This is an important advantage of our model over conventional DL methods. Most DL methods require raw  $k$ -space data to train the network, and this is hard to achieve since most raw data are discarded after the scan (Zbontar et al., 2018). In contrast, DICOM images are relatively much



				Zero-Filled (ZF)	TV	Supervised U-Net	Proposed
Simulation (real)	Uniform 1D	× 4	PSNR [db] SSIM	23.15 ± 1.72 0.571 ± 0.031	27.55 ± 1.60 0.667 ± 0.045	30.58 ± 1.60 0.775 ± 0.036	<b>31.10</b> ± 1.60 <b>0.797</b> ± 0.029
		× 8	PSNR [db] SSIM	22.49 ± 1.69 0.521 ± 0.035	26.35 ± 1.74 0.631 ± 0.053	28.37 ± 1.87 0.671 ± 0.051	<b>29.23</b> ± 1.61 <b>0.742</b> ± 0.035
	Gaussian 1D	× 4	PSNR [db] SSIM	29.20 ± 1.79 0.741 ± 0.039	30.77 ± 1.24 0.752 ± 0.029	32.32 ± 1.22 0.805 ± 0.028	<b>32.89</b> ± 1.25 <b>0.830</b> ± 0.022
		× 8	PSNR [db] SSIM	24.34 ± 1.83 0.594 ± 0.039	28.87 ± 1.56 0.702 ± 0.041	30.76 ± 1.24 0.751 ± 0.028	<b>30.94</b> ± 1.17 <b>0.779</b> ± 0.025
	Gaussian 2D	× 8	PSNR [db] SSIM	20.88 ± 4.72 0.450 ± 0.283	23.19 ± 2.30 0.599 ± 0.082	28.81 ± 1.02 0.701 ± 0.071	<b>29.95</b> ± 2.04 <b>0.724</b> ± 0.028
		× 15	PSNR [db] SSIM	16.37 ± 4.25 0.247 ± 0.299	18.20 ± 2.80 0.456 ± 0.096	26.70 ± 1.58 0.671 ± 0.040	<b>29.58</b> ± 1.47 <b>0.678</b> ± 0.052
Single-coil	Uniform 1D	× 4	PSNR [db] SSIM	26.62 ± 1.93 0.680 ± 0.052	27.55 ± 1.60 0.667 ± 0.045	31.89 ± 1.37 0.808 ± 0.026	<b>31.95</b> ± 1.45 <b>0.810</b> ± 0.034
		× 8	PSNR [db] SSIM	21.55 ± 1.78 0.510 ± 0.037	26.33 ± 1.74 0.631 ± 0.052	29.20 ± 1.48 0.741 ± 0.034	<b>30.21</b> ± 1.38 <b>0.769</b> ± 0.028
	Gaussian 1D	× 4	PSNR [db] SSIM	26.03 ± 1.86 0.714 ± 0.037	30.77 ± 1.24 0.752 ± 0.029	32.86 ± 1.23 <b>0.828</b> ± 0.024	<b>33.08</b> ± 1.19 0.808 ± 0.028
		× 8	PSNR [db] SSIM	22.84 ± 1.66 0.568 ± 0.036	28.87 ± 1.56 0.702 ± 0.041	30.80 ± 1.34 0.777 ± 0.028	<b>31.72</b> ± 1.01 <b>0.779</b> ± 0.034
	Gaussian 2D	× 8	PSNR [db] SSIM	17.65 ± 4.87 0.330 ± 0.320	23.19 ± 2.30 0.599 ± 0.082	28.89 ± 1.06 0.727 ± 0.027	<b>29.45</b> ± 1.18 <b>0.739</b> ± 0.028
		× 15	PSNR [db] SSIM	15.38 ± 3.86 0.232 ± 0.277	18.20 ± 2.80 0.456 ± 0.096	26.40 ± 1.50 0.669 ± 0.032	<b>27.18</b> ± 1.29 <b>0.710</b> ± 0.028
Multi-coil	Uniform 1D	× 4	PSNR [db] SSIM	25.26 ± 2.01 0.725 ± 0.069	28.03 ± 1.69 0.791 ± 0.041	32.18 ± 1.26 0.876 ± 0.028	<b>32.98</b> ± 1.15 <b>0.890</b> ± 0.028
		× 6	PSNR [db] SSIM	23.39 ± 1.92 0.671 ± 0.078	27.01 ± 1.58 0.735 ± 0.048	30.63 ± 1.05 0.846 ± 0.035	<b>30.39</b> ± 1.12 <b>0.867</b> ± 0.031
	Gaussian 1D	× 4	PSNR [db] SSIM	28.73 ± 2.22 0.810 ± 0.051	31.72 ± 1.10 0.839 ± 0.020	33.77 ± 1.17 0.897 ± 0.024	<b>34.55</b> ± 0.93 <b>0.908</b> ± 0.018
		× 6	PSNR [db] SSIM	26.00 ± 2.09 0.748 ± 0.065	29.18 ± 1.84 0.801 ± 0.059	32.04 ± 1.30 0.874 ± 0.031	<b>33.37</b> ± 1.04 <b>0.887</b> ± 0.023
	Gaussian 2D	× 8	PSNR [db] SSIM	20.79 ± 2.71 0.670 ± 0.074	23.81 ± 2.18 0.708 ± 0.059	27.62 ± 1.72 0.810 ± 0.042	<b>31.18</b> ± 1.50 <b>0.834</b> ± 0.021
		× 15	PSNR [db] SSIM	15.79 ± 1.81 0.524 ± 0.071	20.11 ± 3.91 0.585 ± 0.051	24.61 ± 1.54 0.740 ± 0.049	<b>26.10</b> ± 1.98 <b>0.749</b> ± 0.025

Table 1: Quantitative metrics. Numbers are presented as mean value ± unit standard deviation. Numbers in bold face indicate the best metric out of all the methods.

easier to collect, and this enables practitioners to collect large database for training.

### 5.3. Complex-valued Multi-coil Reconstruction

We compare the results of PI reconstruction in Fig. 5. Consistent with the results from the prior sections, our method significantly outperforms other methods, especially good at capturing the high-frequency details of the scan. As can be seen in Table 1, our method, also in the quantitative metrics, consistently outperforms the other methods in all the different sampling types. However, in the case of PI, we do observe some potential limitations of score-POCS. Namely, since we consider stochastic samples from the conditional distribution for each coil, and then take the SSOS of the coil images at the last step to form the reconstruction, we recognize some amount of averaging effect compared to single-coil reconstruction cases. We further discuss the limitations of using score-POCS for PI, in Section 6.4

We emphasize that score-POCS was not trained with multi-coil data, and is yet able to reconstruct PI data with state-of-the-art performance. Our method works with any arbitrary number of coils, without the need to calibrate sensitivity maps, thereby enabling practical application to any type of scans.

### 5.4. Pathology detection

Overall results on the pathology detection task is illustrated in Fig. 6, and the quantitative metric is shown in Fig. 7. The images in Fig. 6 (a-c) were reconstructed from ×4 1D uniform random under-sampling (8% ACS region), (d) is the detection result using fully-sampled data, and (e) is the ground-truth bounding boxes along with the corresponding labels.

The patient scan in the first row of Fig. 6(e) shows grade 1 sprain on posterior cruciate ligament (PCL). Moreover, both on the medial and the lateral side of the cartilage, partial thickness loss/defect is observed. This is accurately captured in Fig. 6 (d), where all three bounding boxes are correctly predicted. Reconstruction with the proposed method come as

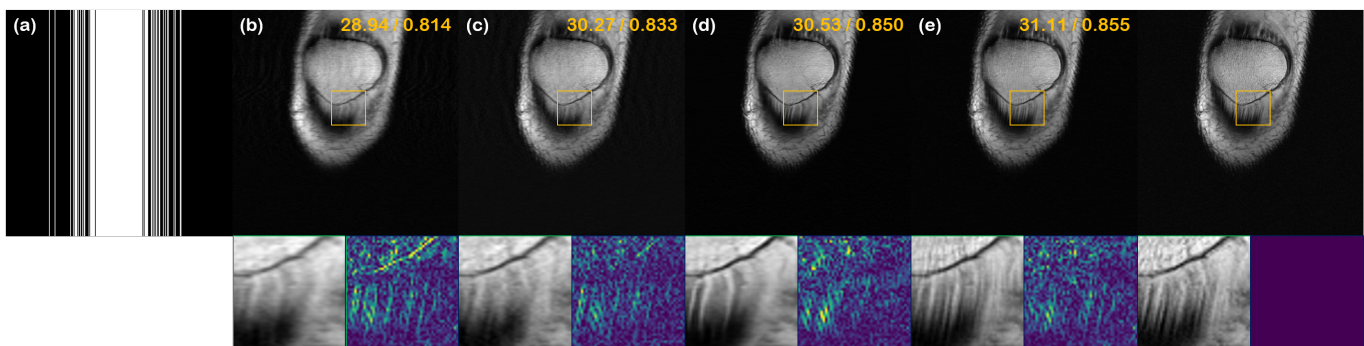


Fig. 5: Multi-coil reconstruction results of  $1D \times 4$  gaussian random sampling. (a) Sub-sampling mask used to generate under-sampled image, (b) zero-filled reconstruction, (c) TV, (d) supervised learning (U-Net), (e) the proposed method, and (f) the ground truth. Green box: Zoom in version of the indicated yellow box, Blue box: Difference magnitude of the inset (In *Viridis* colormap). Yellow numbers in the upper right corner indicate PSNR [db], and SSIM, respectively.

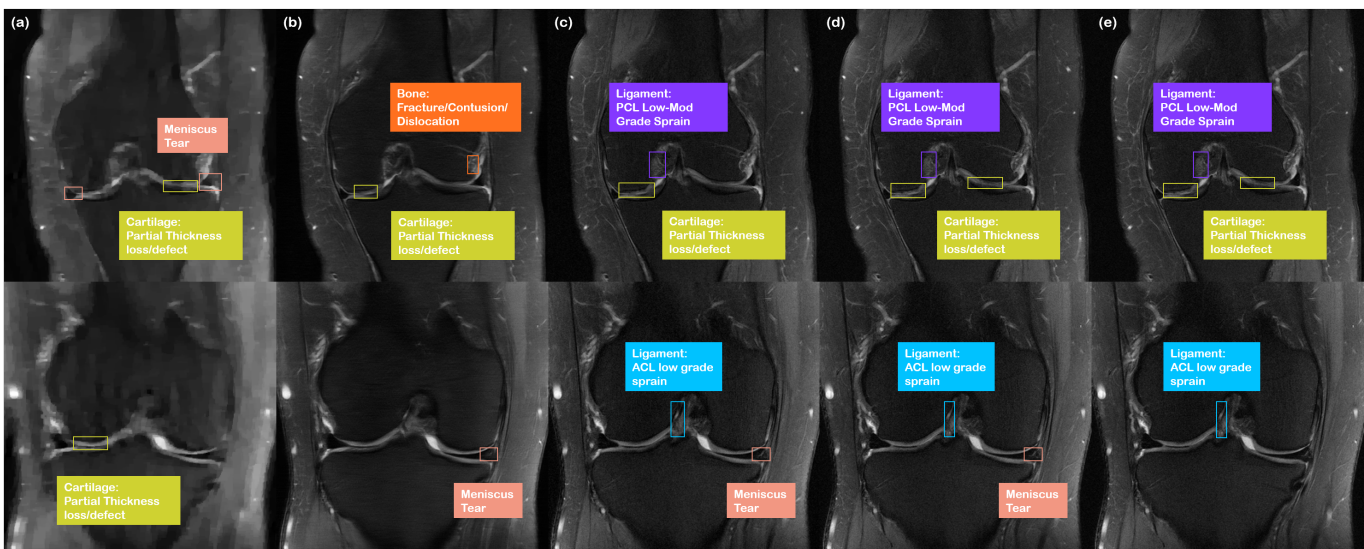


Fig. 6: Results of pathology detection. Detection using (a) TV reconstruction, (b) supervised U-Net, (c) proposed method, (d) fully-sampled images. Ground-truth label for the pathologies are shown in (e).

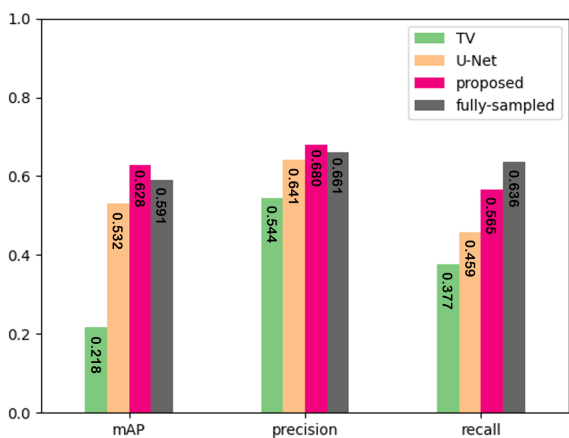


Fig. 7: Quantitative metrics of pathology detection.

close, missing one bounding box for partial cartilage defect (see Fig. 6(c)). Reconstruction with supervised U-Net performs

much worse on this downstream task, missing the PCL sprain (Fig. 6(b)), and also falsely predicting the class of bone fracture/contusion/dislocation. As expected, diagnosis with TV reconstruction performs even worse, falsely predicting meniscus tear on both medial/lateral side.

The patient scan in the second row of Fig. 6(e) show grade 1 sprain on anterior cruciate ligament (ACL). On both fully-sampled data, and reconstruction using score-POCS in Fig. 6(d),(c), respectively, the model correctly predicts ACL low grade sprain, with small differences in the size of the bounding box. Both models also falsely predicts meniscus tear, which seems reasonable given that the model is not perfect. Contrarily, reconstruction using supervised U-Net in Fig. 6(b) does not capture ACL low grade sprain, and only falsely estimates meniscus tear. TV reconstruction in Fig. 6(a) only falsely predicts cartilage loss/defect, missing the true lesion.

As can be seen from standard metrics in Fig. 7, the mAP metric using the fully-sampled data reaches 0.591, which serves as the upper bound for the detection model. Detection using the proposed reconstructions performs on par, or sometimes even better than the fully-sampled reference. Since the model is im-

perfect and the test dataset size is small, this does not mean that the proposed method is better than the fully-sampled data. However, it does mean that reconstruction via proposed method does not hamper the diagnostic capability, which is important in clinical practice. On the other hand, the comparison methods does limit the diagnostic capability, and thus should be considered before usage in clinical practice.

### 5.5. Quantifying uncertainty of the prediction

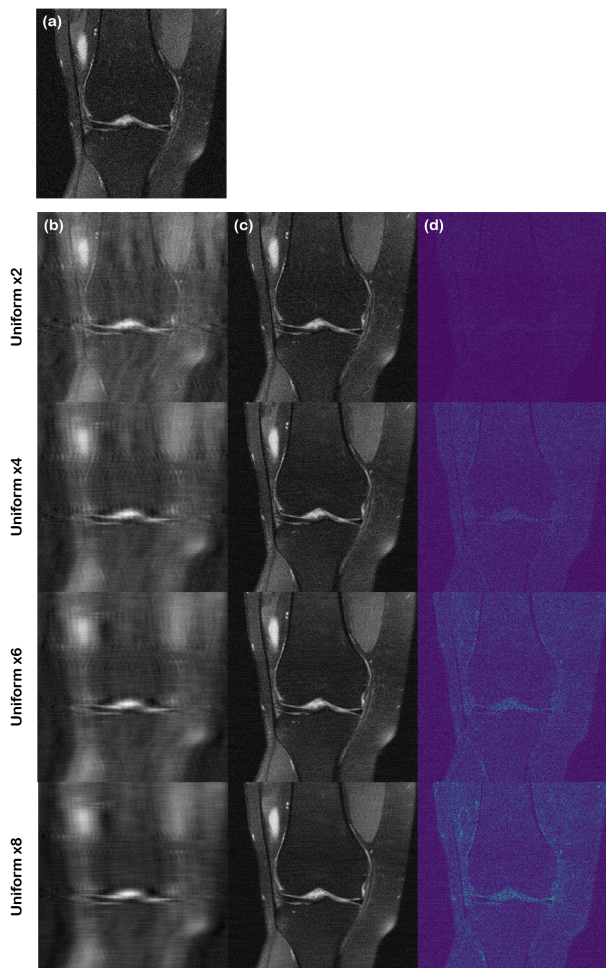


Fig. 8: Quantifying the uncertainty of reconstruction. (a) Ground truth, (b) aliased image from sub-sampling, (c) mean of the reconstruction, (d) standard deviation of the samples: range is set to  $[0, 0.02]$ . (In *Viridis* colormap) From the 1<sup>st</sup> row to the 4<sup>th</sup> row, the acceleration factor grows from  $\times 2$  to  $\times 8$ .

Score-POCS is a generative algorithm, with two sources of stochasticity. First, the sample starts from a randomly sampled vector  $\mathbf{x}_N$ . Second, both predictor and corrector step involve sampling random noise vectors and adding them to the estimate. Therefore, the iterative procedure of the proposed algorithms typically converge to different outcomes.

Due to this generative nature, we can run multiple reconstructions in parallel, and quantify the uncertainty of the prediction, as depicted in Fig. 8. Here, the ground truth, and the aliased images are shown in Fig. 8 (a),(b), respectively. For the experiment, we take batch size of 8, and run the reconstruction in parallel. The mean value of the reconstruction is shown in Fig. 8

(c), and the pixel-wise standard deviation values are shown in Fig. 8 (d). At low acceleration factor ( $\times 2$ ), we see very little variation between the different reconstructions. This indicates high confidence of the model, and hence we can conclude that the reconstruction is exact in all parts of the image. As the acceleration factor is increased, and the degree of aliasing artifacts become severer, we see that the uncertainty increase in specific regions. Potentially, this measure of uncertainty can inform the practitioners on how much they should rely on the reconstruction, thereby deciding whether to use a different diagnostic tool. We additionally provide specific realizations, rather than the mean of the reconstruction, at each acceleration factor in supplementary video 1.

## 6. Discussions

### 6.1. Conditional generation with diffusion models

Score-based diffusion models are now one of the most popular methods in the context of image synthesis, matching the image fidelity of state-of-the-art GANs (Dhariwal and Nichol, 2021), and achieving the state-of-the-art log-likelihood on various datasets (Kingma et al., 2021; Kim et al., 2021). The interest on using these models for conditional image generation is also rising. (Song and Ermon, 2019) first proposed to use score models trained with discrete de-noising score matching for image inpainting. This was further developed in (Song et al., 2021c) to image colorization, and class-conditional image synthesis, using continuous-time score models. The same group published a work for image editing (Meng et al., 2021) using VE-SDEs, which uses a similar algorithm to image inpainting used in (Song and Ermon, 2019; Song et al., 2021c). ILVR (Choi et al., 2021) adopts diffusion models (Ho et al., 2020) for image super-resolution and image translation. All these works require training of a score model irrelevant of the actual objective task, and are thus flexible. Nevertheless, all the prior works have focused on applications where the condition also stays in the image domain, which makes the problem easier to solve. Our method adds further flexibility by showing that conditions can be applied in measurement domains that are not necessarily in the same image domain.

We are aware of one prior work which used denoising score matching for MRI reconstruction (Ramzi et al., 2020). The authors of (Ramzi et al., 2020) use amortized residual de-noising autoencoder (AR-DAE) score matching loss (Lim et al., 2020) to train the score function, then uses annealed Hamiltonian MC (Neal et al., 2011) to perform reconstruction from measurement. However, (Ramzi et al., 2020) reported that their method falls behind supervised learning approaches by a large margin, especially when considering single samples. Moreover, the training methodology in (Ramzi et al., 2020) targets separate channel complex-valued data, which limits their application. Our method, on the other hand, beats neural networks trained with supervision, and requires only the magnitude images for training. It is also notable that the proposed method is applicable to PI.

### 6.2. Energy based models

Energy based models (EBMs) are non-normalized probabilistic models, which have the advantage of circumventing the need to compute the normalizing constant (i.e. the partition function) (Song and Kingma, 2021). Our work relies on denoising score matching to estimate the score, which also belongs to the category of EBMs. There are of course, other ways to train EBMs, and one of the most widely known method other than score matching, is contrastive divergence (CD) (Carreira-Perpinan and Hinton, 2005).

Concurrent to our work, an MR acceleration algorithm utilizing CD was proposed (Guan et al., 2021). This work grounds their method on an EBM, trained with persistent contrastive divergence (PCD), which is a variant of CD using sample buffers (Du and Mordatch, 2019). Specifically, a parameterized energy function  $E_\theta(\cdot)$  is trained such that it takes low values when the input the the function is likely to be in the data distribution, and high values when this is not the case. Once the energy function is trained, one can generate unconditional samples via MCMC, or apply data consistency projection in between the MCMC update steps to sample from a conditional distribution.

This procedure is in fact similar to score-POCS, with the trained functions forming the relationship of  $\nabla_x \log p_\theta(\mathbf{x}) = -\nabla_x E_\theta(\mathbf{x})$ . However, we note two key differences of the proposed method from (Guan et al., 2021). First, in order to train  $E_\theta$  with CD, one has to produce negative samples with MCMC at every iteration of training, which is non-trivial and costly. Several heuristics need to be applied to make the algorithm work. In contrast, training of our score function is much more straightforward and robust, breaking down to an explicit form of the loss function, as formulated in Eq. (13). Second, our method only requires magnitude (DICOM) images for training, whereas (Guan et al., 2021) requires raw data.

### 6.3. Speeding up inference

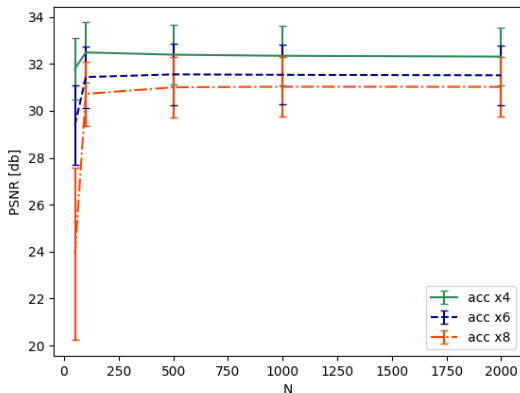


Fig. 9: Tradeoff between number of iterations vs. PSNR [db]. Errorbars indicate unit standard deviation. Sampling scheme used for this ablation study is 1D Gaussian random under-sampling.

One obvious limitation of using score-based diffusion models for image reconstruction, is the time required for inference.

As stated in Section 4.2, it requires about 10 minutes of inference time for using  $N = 2000$  discretization steps. A naïve way for faster inference is to reduce the number of discretization steps, and we provide the trade-off between image quality vs. steps in Fig. 9. Here, we observe that naïvely interleaving the discretization steps work quite well, with minimal compromise in image quality. This is especially the case of low acceleration factors (e.g.  $\times 4$ ), where we achieve highly accurate reconstruction only with 50 iterations. As the acceleration factor gets aggressive, our method typically requires more iterations for maximal performance. However, from the figure, we see that the performance caps at about  $N = 500$ , which is fairly a reasonable amount of iterations in practice. One could possibly adjust this as a hyperparameter on-the-fly, according to the degree of acceleration at hand.

While out of the scope of this work, we suggest two directions of future work for accelerating diffusion models for inverse problems. First, instead of adopting PC sampler, we can also use probability flow ODE sampling introduced in (Song et al., 2021c). Thanks to the use of implicit layers as used in Neural ODE (Chen et al., 2018), one can drastically reduce the time for computation with less compromise. Second, one can reduce the number of computation steps by using denoising diffusion implicit models (DDIM) (Song et al., 2021a), which reduces the stochasticity of the reverse diffusion process. With further studies on accelerating the procedure and rapid development of hardware, we expect to see much faster inference time in the future.

### 6.4. Limitations

As briefly discussed in the results, score-POCS has some limitation when it comes to applying the model to parallel imaging. Individual coil images are assumed to be independent, without the consideration of dependency between each coil. Since we average out the stochastic samples during the SSOS step, the final reconstruction is slightly blurred, with compromised high frequency details. Hence, incorporating coil dependencies into score-POCS so that we can alleviate this effect could be a promising future direction of study.

### 6.5. Broader Impact

Score-POCS can be readily applied to other problems in computational imaging, with well trained score function and the right modifications to the inference procedure. A single score function has already shown broad applicability: SR (Choi et al., 2021; Saharia et al., 2021), image reconstruction, and others. This could potentially shift the current paradigm of deep learning in biomedical imaging. For example, one can train a single score function for the imaging modality, and use it as a universal problem solver, given enough capacity.

## 7. Conclusion

In conclusion, we propose score-POCS, a novel method for accelerated MRI. We train the gradient of the log data distribution with continuous-time denoising score matching using the magnitude data. Using the learned score as the prior, one

can sample from the conditional distribution given the measurement by simply applying data consistency projection at every step. Score-POCS produces reconstructions of high accuracy, whether it be single-coil, or multi-coil case. Comparing to prior arts, we show the superiority of our method both in terms of quality, and practicality.

We believe that our method opens up a new generation of methods for inverse problems in imaging. Direct application of score-POCS to other venues to test the generality is an interesting direction of future research. Other than that, there still remains unanswered questions, for example, reducing the reconstruction speed gap between score-POCS and feedforward neural network approaches. We expect that many interesting questions and answers will be actively discussed in the near future.

## Acknowledgments

This work was supported by the National Research Foundation (NRF) of Korea grant NRF-2020R1A2B5B03001980.

## References

- Arjovsky, M., Chintala, S., Bottou, L., 2017. Wasserstein generative adversarial networks, in: International conference on machine learning, PMLR. pp. 214–223.
- Block, K.T., Uecker, M., Frahm, J., 2007. Undersampled radial MRI with multiple coils. Iterative image reconstruction using a total variation constraint. *Magnetic Resonance in Medicine: An Official Journal of the International Society for Magnetic Resonance in Medicine* 57, 1086–1098.
- Boyd, S., Parikh, N., Chu, E., 2011. Distributed optimization and statistical learning via the alternating direction method of multipliers. Now Publishers Inc.
- Brock, A., Donahue, J., Simonyan, K., 2019. Large scale GAN training for high fidelity natural image synthesis, in: International Conference on Learning Representations (ICLR).
- Carreira-Perpinan, M.A., Hinton, G., 2005. On contrastive divergence learning, in: International workshop on artificial intelligence and statistics, PMLR. pp. 33–40.
- Chen, R.T.Q., Rubanova, Y., Bettencourt, J., Duvenaud, D.K., 2018. Neural ordinary differential equations, in: Advances in Neural Information Processing Systems.
- Choi, J., Kim, S., Jeong, Y., Gwon, Y., Yoon, S., 2021. ILVR: Conditioning method for denoising diffusion probabilistic models, in: Proceedings of the IEEE/CVF International Conference on Computer Vision (ICCV).
- Deshmane, A., Gulani, V., Griswold, M.A., Seiberlich, N., 2012. Parallel mr imaging. *Journal of Magnetic Resonance Imaging* 36, 55–72.
- Dhariwal, P., Nichol, A., 2021. Diffusion models beat GANs on image synthesis. arXiv preprint arXiv:2105.05233 .
- Donoho, D.L., 2006. Compressed sensing. *IEEE Transactions on information theory* 52, 1289–1306.
- Du, Y., Mordatch, I., 2019. Implicit generation and modeling with energy based models, in: Wallach, H., Larochelle, H., Beygelzimer, A., d'Alché-Buc, F., Fox, E., Garnett, R. (Eds.), *Advances in Neural Information Processing Systems*.
- Gal, Y., Ghahramani, Z., 2016. Dropout as a bayesian approximation: Representing model uncertainty in deep learning, in: international conference on machine learning, PMLR. pp. 1050–1059.
- Griswold, M.A., Jakob, P.M., Heidemann, R.M., Nittka, M., Jellus, V., Wang, J., Kiefer, B., Haase, A., 2002. Generalized autocalibrating partially parallel acquisitions (grappa). *Magnetic Resonance in Medicine: An Official Journal of the International Society for Magnetic Resonance in Medicine* 47, 1202–1210.
- Guan, Y., Tu, Z., Wang, S., Liu, Q., Wang, Y., Liang, D., 2021. Mri reconstruction using deep energy-based model. arXiv preprint arXiv:2109.03237
- Ho, J., Jain, A., Abbeel, P., 2020. Denoising diffusion probabilistic models, in: *Advances in Neural Information Processing Systems*, pp. 6840–6851.
- Hyvärinen, A., Dayan, P., 2005. Estimation of non-normalized statistical models by score matching. *Journal of Machine Learning Research* 6.
- Karras, T., Aila, T., Laine, S., Lehtinen, J., 2017. Progressive growing of GANs for improved quality, stability, and variation. arXiv preprint arXiv:1710.10196 .
- Karras, T., Laine, S., Aila, T., 2019. A style-based generator architecture for generative adversarial networks, in: *Proceedings of the IEEE/CVF Conference on Computer Vision and Pattern Recognition*, pp. 4401–4410.
- Karras, T., Laine, S., Aittala, M., Hellsten, J., Lehtinen, J., Aila, T., 2020. Analyzing and improving the image quality of styleGAN, in: *Proceedings of the IEEE/CVF Conference on Computer Vision and Pattern Recognition*, pp. 8110–8119.
- Kendall, A., Gal, Y., 2017. What uncertainties do we need in bayesian deep learning for computer vision? arXiv preprint arXiv:1703.04977 .
- Kim, D., Shin, S., Song, K., Kang, W., Moon, I.C., 2021. Score matching model for unbounded data score. arXiv preprint arXiv:2106.05527 .
- Kingma, D.P., Salimans, T., Poole, B., Ho, J., 2021. Variational diffusion models. arXiv preprint arXiv:2107.00630 .
- Kong, Z., Ping, W., Huang, J., Zhao, K., Catanzaro, B., 2021. Diffwave: A versatile diffusion model for audio synthesis, in: *9th International Conference on Learning Representations, ICLR*.
- Ledig, C., Theis, L., Huszár, F., Caballero, J., Cunningham, A., Acosta, A., Aitken, A., Tejani, A., Totz, J., Wang, Z., et al., 2017. Photo-realistic single image super-resolution using a generative adversarial network, in: *Proceedings of the IEEE conference on computer vision and pattern recognition*, pp. 4681–4690.
- Lim, J.H., Courville, A., Pal, C., Huang, C.W., 2020. AR-DAE: Towards Unbiased Neural Entropy Gradient Estimation, in: *International Conference on Machine Learning, PMLR*. pp. 6061–6071.
- Lustig, M., Donoho, D., Pauly, J.M., 2007. Sparse MRI: The application of compressed sensing for rapid MR imaging. *Magnetic Resonance in Medicine: An Official Journal of the International Society for Magnetic Resonance in Medicine* 58, 1182–1195.
- Lustig, M., Pauly, J.M., 2010. SPIRiT: iterative self-consistent parallel imaging reconstruction from arbitrary k-space. *Magnetic resonance in medicine* 64, 457–471.
- Mason, A., Rioux, J., Clarke, S.E., Costa, A., Schmidt, M., Keough, V., Huynh, T., Beyea, S., 2019. Comparison of objective image quality metrics to expert radiologists' scoring of diagnostic quality of MR images. *IEEE transactions on medical imaging* 39, 1064–1072.
- Meng, C., Song, Y., Song, J., Wu, J., Zhu, J.Y., Ermon, S., 2021. SDEdit: Image synthesis and editing with stochastic differential equations. arXiv preprint arXiv:2108.01073 .
- Neal, R.M., et al., 2011. MCMC using Hamiltonian dynamics. *Handbook of markov chain monte carlo* 2, 2.
- Nichol, A., Dhariwal, P., 2021. Improved denoising diffusion probabilistic models. arXiv preprint arXiv:2102.09672 .
- Niu, C., Song, Y., Song, J., Zhao, S., Grover, A., Ermon, S., 2020. Permutation invariant graph generation via score-based generative modeling, in: *International Conference on Artificial Intelligence and Statistics, PMLR*. pp. 4474–4484.
- Oh, G., Sim, B., Chung, H., Sunwoo, L., Ye, J.C., 2020. Unpaired deep learning for accelerated mri using optimal transport driven cyclegan. *IEEE Transactions on Computational Imaging* 6, 1285–1296.
- Parisi, G., 1981. Correlation functions and computer simulations. *Nuclear Physics B* 180, 378–384.
- Paszke, A., Gross, S., Massa, F., Lerer, A., Bradbury, J., Chanan, G., Killeen, T., Lin, Z., Gimelshein, N., Antiga, L., et al., 2019. Pytorch: An imperative style, high-performance deep learning library. *Advances in neural information processing systems* 32, 8026–8037.
- Pruessmann, K.P., Weiger, M., Scheidegger, M.B., Boesiger, P., 1999. Sense: sensitivity encoding for fast mri. *Magnetic Resonance in Medicine: An Official Journal of the International Society for Magnetic Resonance in Medicine* 42, 952–962.
- Ramzi, Z., Rémy, B., Lanusse, F., Starck, J.L., Ciuciu, P., 2020. Denoising score-matching for uncertainty quantification in inverse problems. arXiv preprint arXiv:2011.08698 .
- Ronneberger, O., Fischer, P., Brox, T., 2015. U-net: Convolutional networks for biomedical image segmentation, in: *International Conference on Medical image computing and computer-assisted intervention, Springer*. pp. 234–

- 241.
- Saharia, C., Ho, J., Chan, W., Salimans, T., Fleet, D.J., Norouzi, M., 2021. Image super-resolution via iterative refinement. arXiv preprint arXiv:2104.07636 .
- Samsonov, A.A., Kholmovski, E.G., Parker, D.L., Johnson, C.R., 2004. POC-SENSE: POCS-based reconstruction for sensitivity encoded magnetic resonance imaging. *Magnetic Resonance in Medicine: An Official Journal of the International Society for Magnetic Resonance in Medicine* 52, 1397–1406.
- Sohl-Dickstein, J., Weiss, E., Maheswaranathan, N., Ganguli, S., 2015. Deep unsupervised learning using nonequilibrium thermodynamics, in: *International Conference on Machine Learning*, PMLR. pp. 2256–2265.
- Song, J., Meng, C., Ermon, S., 2021a. Denoising diffusion implicit models, in: *9th International Conference on Learning Representations, ICLR*.
- Song, Y., Durkan, C., Murray, I., Ermon, S., 2021b. Maximum likelihood training of score-based diffusion models. arXiv e-prints , arXiv–2101.
- Song, Y., Ermon, S., 2019. Generative modeling by estimating gradients of the data distribution, in: *Advances in Neural Information Processing Systems*.
- Song, Y., Ermon, S., 2020. Improved techniques for training score-based generative models, in: *Advances in Neural Information Processing Systems*, pp. 12438–12448.
- Song, Y., Garg, S., Shi, J., Ermon, S., 2020. Sliced score matching: A scalable approach to density and score estimation, in: *Uncertainty in Artificial Intelligence*, PMLR. pp. 574–584.
- Song, Y., Kingma, D.P., 2021. How to train your energy-based models. arXiv preprint arXiv:2101.03288 .
- Song, Y., Sohl-Dickstein, J., Kingma, D.P., Kumar, A., Ermon, S., Poole, B., 2021c. Score-based generative modeling through stochastic differential equations, in: *9th International Conference on Learning Representations, ICLR*.
- Tancik, M., Srinivasan, P.P., Mildenhall, B., Fridovich-Keil, S., Raghavan, N., Singhal, U., Ramamoorthi, R., Barron, J.T., Ng, R., 2020. Fourier features let networks learn high frequency functions in low dimensional domains. arXiv preprint arXiv:2006.10739 .
- Vincent, P., 2011. A connection between score matching and denoising autoencoders. *Neural computation* 23, 1661–1674.
- Wang, S., Su, Z., Ying, L., Peng, X., Zhu, S., Liang, F., Feng, D., Liang, D., 2016. Accelerating magnetic resonance imaging via deep learning, in: *2016 IEEE 13th international symposium on biomedical imaging (ISBI)*, IEEE. pp. 514–517.
- Yaman, B., Hosseini, S.A.H., Moeller, S., Ellermann, J., Uğurbil, K., Akçakaya, M., 2020. Self-supervised learning of physics-guided reconstruction neural networks without fully sampled reference data. *Magnetic resonance in medicine* 84, 3172–3191.
- Zbontar, J., Knoll, F., Sriram, A., Murrell, T., Huang, Z., Muckley, M.J., Defazio, A., Stern, R., Johnson, P., Bruno, M., et al., 2018. fastMRI: An open dataset and benchmarks for accelerated MRI. arXiv preprint arXiv:1811.08839 .
- Zhang, R., 2019. Making convolutional networks shift-invariant again, in: *International conference on machine learning*, PMLR. pp. 7324–7334.
- Zhao, R., Yaman, B., Zhang, Y., Stewart, R., Dixon, A., Knoll, F., Huang, Z., Lui, Y.W., Hansen, M.S., Lungren, M.P., 2021. fastmri+: Clinical pathology annotations for knee and brain fully sampled multi-coil mri data. arXiv preprint arXiv:2109.03812 .